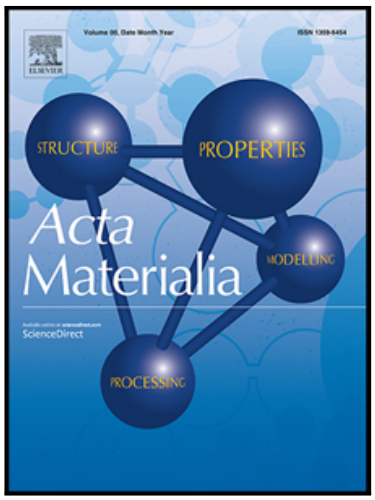

Coarsening of dendrites in solution-based freeze-cast ceramic systems

Noriaki Arai , Tiberiu Stan , Sophie Macfarland , Peter W. Voorhees , Nancy S. Muyanja , Ashwin J. Shahani , Katherine T. Faber

PII: S1359-6454(21)00419-5
DOI: https://doi.org/10.1016/j.actamat.2021.117039
Reference: AM 117039

To appear in: *Acta Materialia*

Received date: 23 March 2021
Revised date: 21 May 2021
Accepted date: 27 May 2021

Please cite this article as: Noriaki Arai , Tiberiu Stan , Sophie Macfarland , Peter W. Voorhees , Nancy S. Muyanja , Ashwin J. Shahani , Katherine T. Faber , Coarsening of dendrites in solution-based freeze-cast ceramic systems, *Acta Materialia* (2021), doi: https://doi.org/10.1016/j.actamat.2021.117039

Coarsening of dendrites in solution-based freeze-cast ceramic systems

Noriaki Arai[a]*, Tiberiu Stan[b]*, Sophie Macfarland[b], Peter W. Voorhees[b], Nancy S. Muyanja[c], Ashwin J. Shahani[d], Katherine T. Faber[a†]

[a] Division of Engineering & Applied Sciences, California Institute of Technology, Pasadena, CA 91125, USA

[b] Department of Materials Science and Engineering, Northwestern University, Evanston, IL 60208, USA

[c] Michigan Center for Materials Characterization, University of Michigan, Ann Arbor, MI 48109, USA

[d] Department of Materials Science and Engineering, University of Michigan, Ann Arbor, MI 48109, USA

*Co-first authors

[†]Corresponding author:

Address: MC 138-78, California Institute of Technology, Pasadena, CA 91125, USA

Email address: ktfaber@caltech.edu

Phone: 626-395-4448

Abstract

The morphologies of freeze-cast materials are typically controlled and tuned by adjusting the freezing-front velocity and temperature gradient. Recently it has been demonstrated that coarsening, similar to that commonly practiced in alloy systems, is

also effective for morphological control in freeze-cast materials. However, the underlying coarsening mechanisms and their effect on microstructure evolution are largely unknown. In this study, frozen preceramic polymer/cyclohexane solutions were coarsened at 2 °C and 4 °C for up to 5 h, and the resulting morphologies were characterized using scanning electron microscopy, mercury intrusion porosimetry, and X-ray computed tomography. During coarsening the microstructure evolved from dendritic (primary and secondary pores) to honeycomb-like (large open channels with flat walls). The size of both primary and secondary pores increased linearly with the cube root of coarsening time, consistent with dendritic coarsening in alloy systems. Other important metrics such as primary dendrite spacing, dendrite growth directionality, and the effect of coarsening on the pore-ceramic interface area are reported. These findings provide novel insights into coarsening of freeze-cast systems and can lead to new avenues for microstructure tailorability.

Keywords: ice-templating, Ostwald ripening, porous materials, preceramic polymers, X-ray computed tomography

1. Introduction

Porous ceramics are receiving considerable attention for their hardness, chemical inertness, high temperature resistance, corrosion resistance and wear resistance while providing pore networks suitable for insulation, bio-medical implants, and filtration [1]. Since each application requires specific microstructures, there is growing research on porous ceramic processing techniques [2,3]. Of the variety of methods to produce porous materials, freeze casting is one which provides exceptional tunability, not only with respect to pore directionality and alignment, but also for pore

size, pore morphology, connectivity and tortuosity. In this method, a suspension or solution is directionally frozen such that growing crystals reject suspended particles or segregate the dissolved preceramic polymer. A sublimation step that follows removes solvent crystals, leaving pores in materials, and a subsequent sintering or pyrolysis step yields a porous solid. Pores are typically tuned by the concentration of suspension/solution, solvents, solidification parameters (freezing front velocity, temperature gradient, etc.), and additives. Pore size can be controlled by the freezing front velocity [4] and the concentration of particles or solute [5], and generally ranges from ~300 nm to ~500 µm [6,7]. Furthermore, pore morphology can be controlled by choice of solvents [8], temperature gradient [9], additives [10], and by modifying freeze casting techniques such as two-stage freeze casting [11] and magnetic freeze casting [12]. This tailorability in pore size and morphology leads to potential applications of freeze-cast ceramics that include bone tissue engineering [13,14], supercapacitors [15], filtration [16], cryogenic wicking [17], and medical diagnostic devices [18]. These studies focused on changing the above parameters to control the initial crystal growth step. In our study, we use coarsening as a post-crystal growth process to alter both pore size and morphology.

Solidification is the foundation upon which freeze casting is built. A study by Miller et al. demonstrated that classical solidification theory can be successfully applied to describe the relationship between pore size, temperature gradient, and freezing front velocity in freeze-cast systems [19]. Coarsening, also known as Ostwald ripening, is a phenomenon which occurs in multi-phase systems such as alloys and metal oxides [20], and is driven by the reduction of interfacial energy to minimize the free energy of the

system. The total interfacial area in a system is decreased through mass transport, which is driven by the concentration gradient resulting from a large interfacial mean curvature to a small interfacial mean curvature due to the Gibbs-Thomson effect (1):

$$C_L = C_\infty + l_c H \qquad (1)$$

where $$H = \frac{1}{2}(\kappa_1 + \kappa_2)$$

and C_L is the composition of liquid at the solid-liquid interface, C_∞ is the composition of the liquid at flat solid-liquid interface, l_c is the capillary length and H is the mean curvature of interfaces. H is determined by the two principle curvatures, κ_1 and κ_2. Coarsening of alloys has been extensively studied in systems ranging from simple spherical geometries [21] to complex interconnected structures such as dendrites characterized by tree-like arms [22,23]. Coarsening studies span theory [24] to modeling [25,26] to *in-situ* and *ex-situ* experimental studies [27–32]. Two important results on coarsening of dendrites are highlighted here. First, Bower et al. found that secondary dendritic arm spacing (λ_2) increases with coarsening time as:

$$\lambda_2 \sim t_f^{1/3} \qquad (2)$$

where t_f is the local solidification time [33]. Second, Kammer et al. reported that dendritic structures turned into cylinders or cylindrical-like shapes after coarsening Pb-Sn alloys at 185 °C for four days, and Al-Cu alloys at 553 °C for three weeks [23].

Studies of coarsening in freeze-cast systems are limited [34–36]. Pawelec et al. investigated low-temperature ice annealing in a collagen suspension, and observed coarsened microstructures after twenty hours of annealing at temperatures below -20 °C [36]. Liu et al. examined coarsening of camphene crystals in freeze casting of bioactive glass to obtain a controllable pore diameter, ranging from 15 μm to 160 μm

[35]. Both studies only reported pore sizes and provided a qualitative image analysis. Hence, there remains a gap between these observations and what is understood at a fundamental level in alloy systems. Furthermore, these studies were conducted using suspension-based freeze casting. The use of suspended colloids or powders and dissolved additives makes understanding the coarsening mechanisms and comparing them to alloy systems very difficult, whereas a solution contains a preceramic polymer and a small amount of the cross-linking agent, both of which are dissolved in a solvent.

Our study focuses on solution-based freeze casting and investigates the evolution of dendrites during isothermal coarsening. Morphological evolution was first characterized using scanning electron microscopy (SEM) and mercury intrusion porosimetry (MIP). To gain further insights into the coarsening processes of freeze-cast systems in three dimensions, X-ray computed tomography (XCT) was used to quantitatively analyze the complex pore morphologies and directionality of primary dendrites using interfacial shape distributions (ISDs) and interfacial normal distributions (INDs), respectively [37]. By coupling the three characterization techniques, our study provides new insights into coarsening of freeze-cast systems, allows for comparisons with coarsening in alloy systems, and offers an additional means for pore network tailorability.

2. Experimental procedures

2.1 Processing

A polysiloxane (CH_3-$SiO_{1.5}$, Silres® MK Powder, Wacker Chemie) preceramic polymer was dissolved in cyclohexane (C_6H_{12}, Sigma-Aldrich), with a composition of

preceramic polymer of 20 wt.%. After a homogeneous solution was obtained by stirring, a cross-linking agent (Geniosil® GF 91, Wacker Chemie) was added in concentrations of 1 wt.% and stirred for an additional 5 min. Subsequently, the polymer solution was degassed for 10 min to prevent air bubbles during freezing. The polymer solution was poured into a cylindrical glass mold (h = 20 mm, Ø = 24 mm) and placed on a PID-controlled thermoelectric plate. A second PID-controlled thermoelectric plate was placed on top of the mold to maintain a constant freezing front velocity and temperature gradient (Fig. 1). A cold finger, smaller than the inner diameter of the mold, was inserted into the top of the mold creating a reservoir for solution as the solution shrunk during the freezing. The freezing front velocity was measured using a camera and intervalometer. The temperature gradient, G was determined by the following equation:

$$G = \frac{T_t - T_f}{d} \qquad (3)$$

where T_t is the temperature of the top cold finger, T_f is the temperature of freezing front and d is the distance between the top cold finger and the freezing front. The temperature of the freezing front was assumed to be at the liquidus temperature of the solution, which was measured by Naviroj [5] as 4.2 °C. All samples were frozen at freezing front velocities of 15 μm/s, and temperature gradients of 2.5 K/mm to maintain homogeneous pore structures.

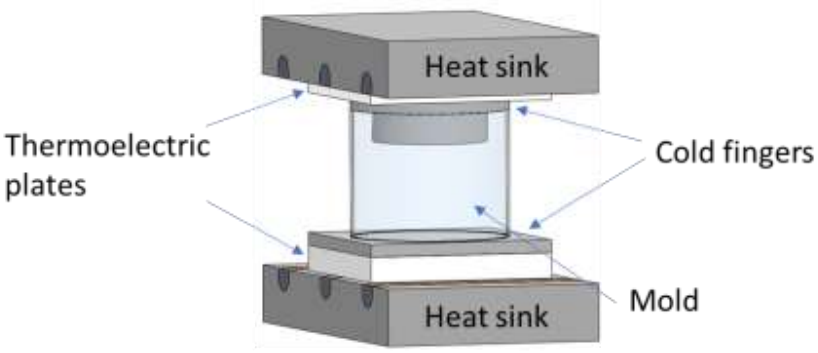

Fig. 1. Schematic of the gradient-controlled freeze casting setup

To induce coarsening after freezing was completed, the top and bottom thermoelectrics were set to temperatures close to the melting temperature of the solution (2 °C or 4 °C) and held for up to 5 h. After coarsening, the samples were cooled to -30 °C to fully re-freeze. Once frozen, the samples were placed in a freeze drier where the solvent crystals were completely sublimated. After freeze drying, the polysiloxane green bodies were pyrolyzed in argon at 1100 °C for 4 h with a 2 °C/min ramp rate to convert the preceramic polymer into silicon oxycarbide (SiOC). This resulted in a porosity of ~77%. The resulting 9.5 mm tall and 18 mm diameter samples are composed of SiOC ceramic with dendritic pores.

2.2 Characterization

Pore structures were observed using scanning electron microscopy (SEM; ZEISS 1550VP). Longitudinal (plane parallel to the freezing direction) and transverse (plane perpendicular to the freezing direction) cross-sections were prepared using a diamond saw and imaged. Pore size distributions were measured using mercury intrusion porosimetry (MIP) using a Micromeritics Auto Pore IV instrument. All samples for MIP

were machined with a core drill (Ø = 15.9 mm) to remove the edges, and a ~1.8 mm disk was sectioned from the center of the sample.

X-ray computed tomography (XCT) was performed on selected samples to quantitatively measure sample morphologies in three dimensions via absorption contrast tomography on a laboratory X-ray microscope (XCT; Zeiss Xradia Versa 520, Carl Zeiss AG, Oberkochen, Germany) at the Michigan Center for Materials Characterization. Three samples (height = ~5 mm, Ø = ~1.2 mm) were chosen for this analysis: a control sample without coarsening, one coarsened at 2 °C for 1 h and another coarsened at 4 °C for 3 h. During the XCT measurement, each sample was positioned 5.1 mm in front of a polychromatic X-ray source tuned to 40 kV, 3 W and 75 µA. The X-ray beam interacted with a sample volume of 1025 µm x 1132 µm x 1090 µm. A series of 1601 X-ray projection images was collected at 0.2° intervals while the sample rotated through 360° at exposure times of 1.1 s per projection. A scintillator downstream from the sample converted the X-ray projection images into visible light images and a 4X objective lens magnified the visible light image before coupling it to the 2k x 2k CCD detector placed 23.5 mm away from the sample. With the CCD operating at a pixel binning of 2, a scan pixel size of 1.2 µm/voxel was achieved. The collected projection images were reconstructed using a filtered back projection algorithm in the Scout and Scan software provided by Zeiss Xradia Inc. to create a virtual 3D volume of the sample. Phase retrieval [38] was not necessary because there was sufficient contrast between the SiOC matrix and the pore network (see supplementary Fig. 1).

The control sample (without coarsening) was segmented using Otsu's method [39] in MATLAB. Although Otsu's method is computationally straightforward and the

preferred segmentation approach, it was not successful on the 2 °C and 4 °C coarsened datasets due to the presence of debris and bright spot artifacts at random sections throughout the reconstructions. The coarsened datasets were instead segmented using a convolutional neural network (CNN) machine learning approach as described by Stan et al. [40,41]. First, 35 representative slices were selected from each reconstruction to include sections of debris and bright spots and split into three categories: 20 images for training, 10 images for validation, and 5 images for testing. Each image was then segmented using a combination of thresholding and manual cleaning using the GIMP software. These ground truth segmentations, along with the original images, were used to train CNNs with the SegNet architecture using the PyTorch framework. Each CNN was trained for 100 epochs on the Quest supercomputer at Northwestern University. The CNNs each achieved 99.4 % segmentation accuracy when applied to test images from the 2 °C and 4 °C coarsened datasets.

MATLAB was used for all post-segmentation analysis. It was found empirically that 120 µm thick sections (100 z-slice images) of each XCT dataset were large enough to capture the defining morphological features, yet small enough to be computationally manageable. All three segmented datasets were meshed, then smoothed using the "smoothpatch" function [42]. The control and 2 °C datasets were smoothed for 5 iterations, while the coarser 4 °C dataset was smoothed for 15 iterations. Principle curvatures (κ_1 and κ_2) and normal vectors were calculated at each of the triangular mesh faces. Their respective frequencies within the microstructures are plotted as interface shape distributions (section 3.5) and interface normal distributions (section 3.6).

3. Results

3.1 Pore structure

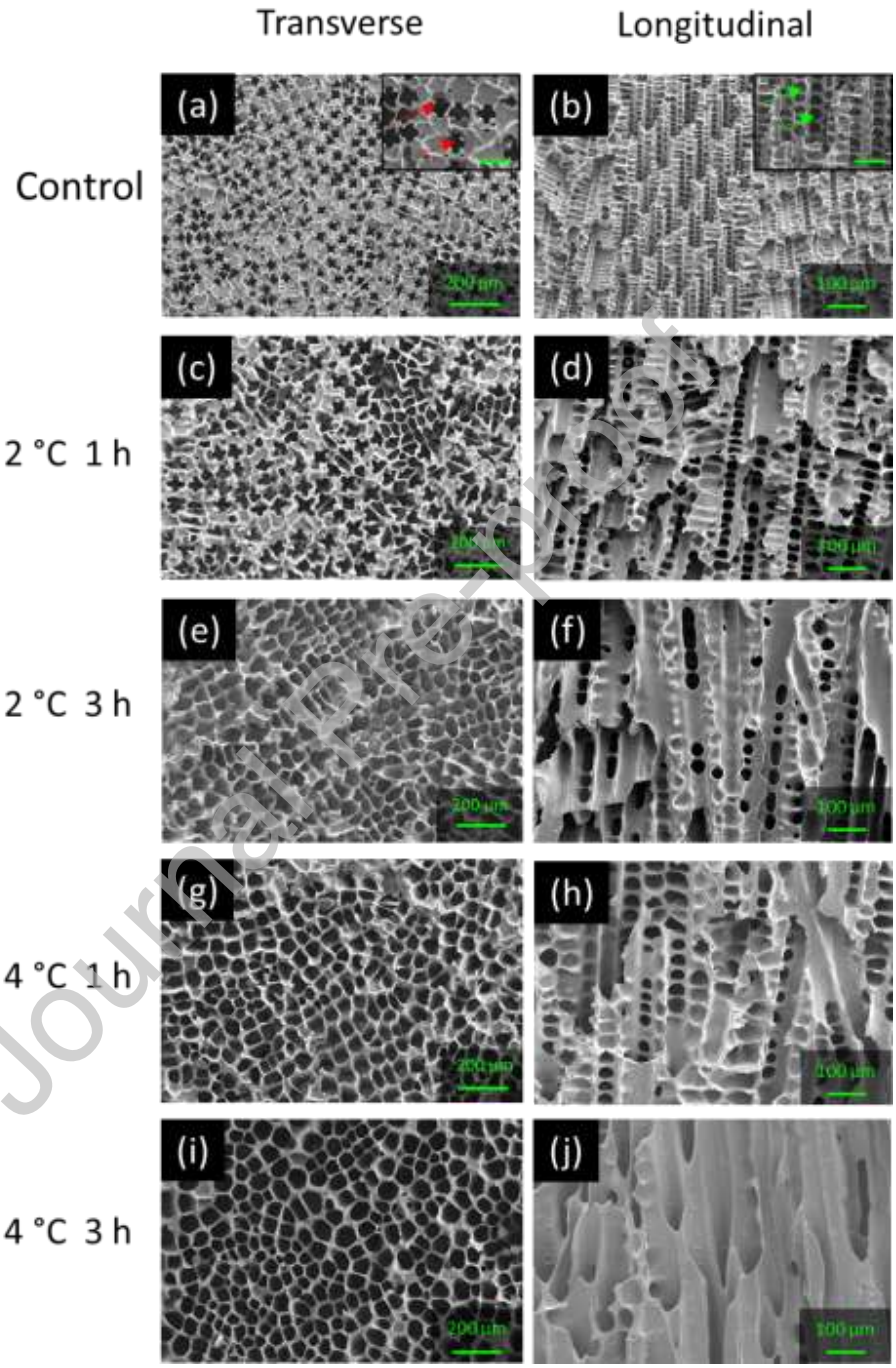

Fig. 2. SEM images showing (a,b) control sample, (c,d) sample coarsened at 2 °C for 1 h, (e,f) 2 °C for 3 h, (g,h) 4 °C for 1 h, and (i,j) 4 °C for 3 h. The inset image in (a) shows

a higher magnification view of the primary pores (red arrows), while the inset image in (b) shows a higher magnification view of the secondary pores (green arrows). The inset scale bars in (a) and (b) are 60 μm and 40 μm, respectively. Transverse images and longitudinal images show cross-sections perpendicular and parallel to the freezing direction, respectively.

Fig. 2 shows a series of SEM images of dendritic pores as a function of coarsening treatment beginning with the as-cast and pyrolyzed control sample (Figs. 2a and b). Since cyclohexane dendrites template the pores, the pores (appearing black in SEM images) are the negatives of dendrites [43,44]. The transverse image (perpendicular to the solidification direction) in Fig. 2a shows primary pores templated by primary dendrites (red arrows), and secondary pores templated by secondary dendrite arms. Tertiary pores are occasionally observed in regions where primary interpore spacings are large (supplementary Fig. 2). The four-fold symmetry of dendritic pores is consistent with the cubic structure of cyclohexane crystals [43,45]. The longitudinal image (approximately parallel to the solidification direction) in Fig. 2b shows the cutaway view of dendritic pores, where the green arrows in the inset image indicate secondary pores that were formerly secondary dendrite arms. When the dendrites are coarsened at 2 °C for 1 h, there is an increase in both primary and secondary pore size as shown in Figs. 2c and d. After three hours of coarsening at 2 °C, the transverse image shows larger domains of honeycomb-like structures (Fig. 2e) although the secondary pores are still present as noted in the longitudinal image (Fig. 2f).

When the coarsening temperature is increased to 4 °C, morphological evolution proceeds at a higher rate (Figs. 2g-j). Coarsening for one hour yields larger domains of the honeycomb structure in the transverse direction (Fig. 2g) while secondary pores are still noted in the longitudinal image (Fig. 2h). After three hours of coarsening at 4 °C, the majority of secondary pores disappear in the longitudinal image (Fig. 2j), producing a largely honeycomb-like structure. The morphological evolution of dendritic pores observed in this solution-based freeze casting agrees with what has been reported in coarsening of dendrites in alloys [23,29], where dendrites evolve into cylindrical-like morphologies. A longer coarsening time (five hours) at 4 °C was also investigated, but there were only minor morphological changes (supplementary Fig. 3). These minor changes can be attributed to the decreasing diffusion coefficient of preceramic polymer as gelation of the solution starts around five to six hours, as indicated by its viscosity.

3.2 Pore size distribution

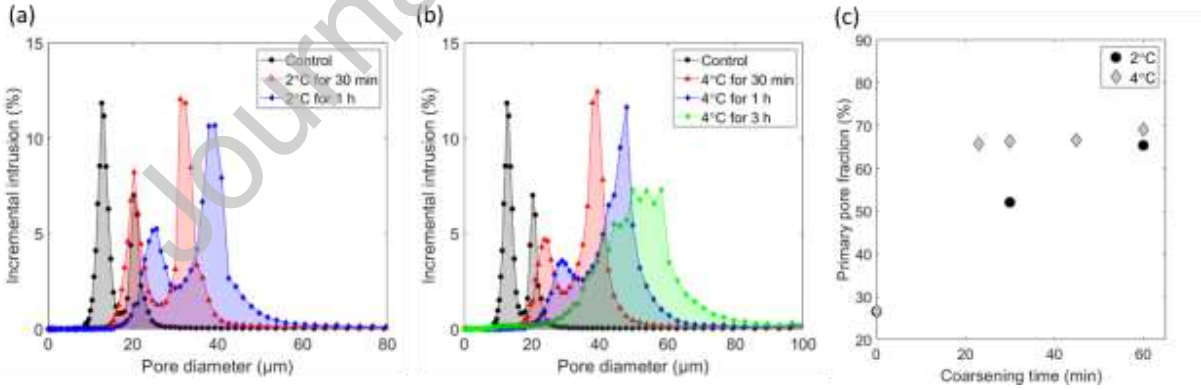

Fig. 3. Pore size distribution data of samples coarsened at (a) 2 °C and (b) 4 °C. (c) Plot showing primary pore fraction as a function of coarsening time.

The pore diameters and their frequencies throughout the microstructures as measured using MIP for each coarsening temperature are shown in Fig. 3. Fig. 3a shows the pore size distribution from samples coarsened at 2 °C compared to the control sample. All samples exhibit a bimodal distribution, which are attributed to the presence of large primary pore diameters and small secondary pore diameters. As the samples are coarsened, primary pores and secondary pores became larger with the distributions shifting to the right, consistent with SEM images. Dendritic structures typically have a secondary pore volume that exceeds the primary pore volume because of the large number of secondary arms that grow from each primary dendrite [8]. In contrast, in the current coarsening studies, not only does the pore size distribution shift to larger pores, but also the primary pore volume eclipses the secondary pore volume.

The same trend was observed in samples coarsened at 4 °C (Fig. 3b). For the sample coarsened for one hour, the distributions for primary and secondary pores overlap. This trend is most pronounced in the sample coarsened for three hours. Distinct bimodal distributions disappear in favor of a unimodal distribution. This corresponds well with Figs. 2i and 2j in which most secondary pores disappear, yielding the honeycomb-like structure. The primary pore volume fraction were calculated using peak fitting [46] and plotted as a function of coarsening time in Fig. 3c. The primary pore fraction increased by 146 % and 160 % after coarsening for 1 h at 2 °C and 4 °C, respectively.

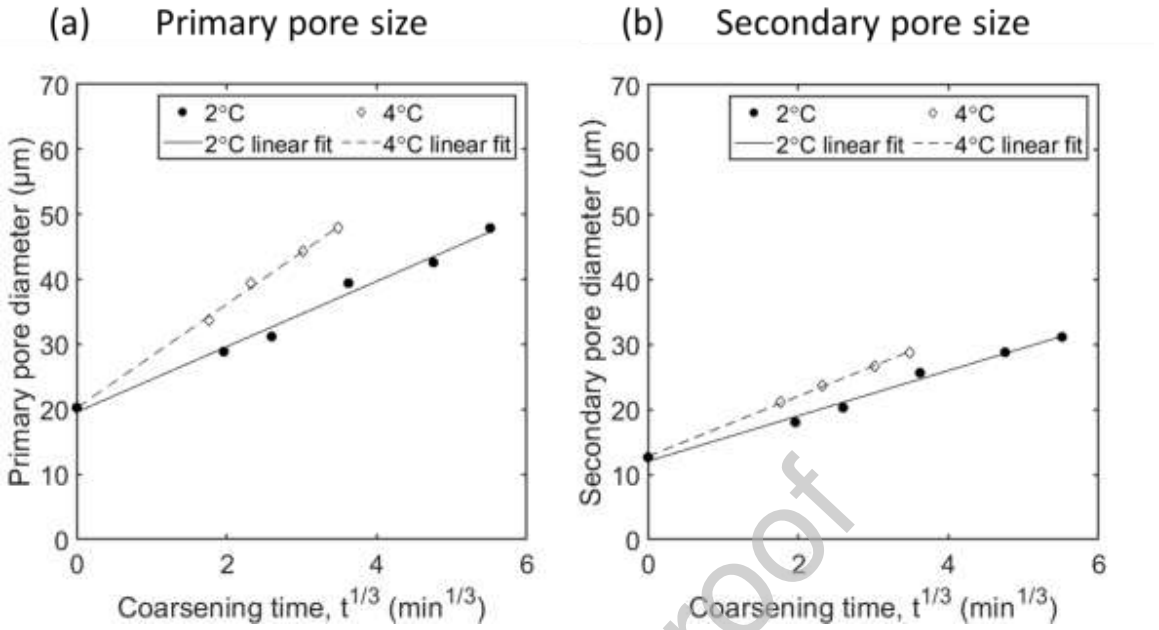

Fig. 4. (a) Primary pore size and (b) secondary pore size as a function of the cube root of adjusted coarsening time at different coarsening temperatures.

To more easily compare the coarsening behavior of freeze-cast systems with typical alloy systems (Eqn. 2), primary and secondary pore sizes are plotted as a function of the cube root of adjusted coarsening time ($t^{1/3}$) in Figs. 4a and 4b. The adjusted coarsening time is defined as the time interval over which the thermoelectric plates are at the prescribed coarsening temperature, adjusted by the time it took the frozen sample to reach the equilibrium coarsening temperature. In Figs. 4a and 4b, the peak values from the pore size distributions are plotted as representatives of primary and secondary pore sizes. The $t^{1/3}$ dependence is obeyed for both coarsening temperatures, consistent with coarsened dendrites in alloy systems. Typically, only the dependence of the secondary arm spacing on $t^{1/3}$ is reported [33], but it was found in the current study that the diameters of primary dendrites follow a similar trend. The

slopes of the linear fit are summarized in Table 1. As expected, the slopes increase with temperature, in agreement with the observations of dendritic coarsening in Al-Cu-Mn alloys by Chen and Kattamis [47]. For both coarsening temperatures, the slopes of lines for the primary dendrites are larger than those for the secondary arms of dendrites. Specifically, increasing the coarsening temperature increased the slope for primary pores by a factor of 1.6, whereas the slope increased for secondary pores by a factor of 1.3, indicating that primary dendrites coarsen at a slightly faster rate. This difference is attributed to a secondary arm retraction coarsening mechanism [48,49]. During coarsening, many secondary arms retract toward their base, leading to overall increases in both primary and secondary arm diameters.

Table 1. The slope of linear fit from Fig. 4.

Coarsening temperature	Primary pore slope [$\mu m/min^{1/3}$]	Secondary pore slope [$\mu m/min^{1/3}$]
2 °C	5.0 ± 0.3	3.5 ± 0.2
4 °C	8.0 ± 0.2	4.6 ± 0.1

3.3 Coarsening mechanisms in solution-based freeze casting

Fig. 5 shows three-dimensional reconstructions of the un-coarsened control sample (Fig. 5a), the sample coarsened at 2 °C for 1 h (Fig. 5b), and the sample coarsened at 4 °C for 3 h (Fig. 5c). The datasets are plotted such that the solidification direction is pointing out of the page. The corresponding videos of the structures rotating as viewed from a 45° tilt away from the solidification direction are available in the supplementary materials (Supplementary Video 1, 2, 3). Subsections from each of the

three reconstructions are shown in Figs. 5d-f. Corresponding videos of the subsections rotating are also available in the supplementary materials (Supplementary Video 4, 5, 6). The sides of the interfaces that face the solid SiOC are colored dark gray. The sides of the interfaces that face the porous dendrites are colored according to their normalized mean curvature H/S_s. The specific interface area (S_s) is a characteristic microstructural length scale and is the total interface area divided by the total pore (dendrite) volume in the dataset. Normalizing curvatures by S_s is used to facilitate visual comparison between coarsening datasets and to check for self-similarity (see section 3.4 and reference [50]).

A significant change in pore size and pore morphology is observed by comparing the microstructures in Fig. 5, consistent with the previous SEM and MIP characterizations. The control sample (Figs. 5a and d) has patches with large positive mean curvature (yellow) mainly located at the tips and sides of the secondary pores, and patches with small and negative mean curvature (purple) primarily present at the roots of secondary pores. The interfaces with nearly zero mean curvature (light blue and light green) are at the flat sections along secondary pores.

The control sample has two distinct domains of dendritic pores that vary by dendritic pore spacing. The white plus-shaped areas at the bottom right of Fig. 5a are one domain where primary dendrites are well-aligned with the temperature gradient. This domain has interpore spacing of ~40 μm. The rest of the sample has misaligned primary dendrites with larger interpore spacing (~70 μm separation). The misalignment is measured as ~28° from the temperature gradient and confirmed using interface normal distributions (section 3.5). These observations are consistent with other studies

which show that primary dendrite spacing generally increases with misorientation [51–53].

Morphological changes in the dendritic pore network and secondary arms are evident when comparing the three XCT datasets. Most secondary pores in the control sample have capped ends such that each dendritic pore was isolated from adjacent dendritic pores, as shown in the SEM image (Fig. 2b). In the 2 °C sample, some of the secondary pore caps remain (white arrows in Fig. 5e). However, some caps are lost during coarsening resulting in connections between secondary pores and in the formation of ceramic ligatures (red arrow in Fig. 5e). The sample coarsened at 4 °C for 3 h no longer contains secondary pores and the microstructure is instead primarily composed of larger channels with nearly-flat sides, as indicated by the green and light-blue coloring in Fig. 5f. Areas of higher curvature (yellow stripes in Fig. 5f) are present where the flatter sections intersect.

The color-coded 3D reconstructions also provide insights into why dendritic morphologies evolve to honeycomb-like structures through coarsening. Large positive mean curvatures are preferentially found at the tips and sides of secondary pores. In contrast, small and negative curvatures are found at the roots of the secondary pores, where there is a high preceramic polymer concentration. During coarsening some regions of the dendritic structures melt and re-dissolve the preceramic polymer. This leads to liquid being present in the interdendritic regions. As a result, near these interface regions, there is a high solvent content and equivalently low preceramic polymer concentration due to the Gibbs-Thomson effect. Hence, the preceramic polymer diffuses from the roots of secondary arms to the tips and sides of secondary

arms, which dissolves the tips and sides but solidifies the roots. This mechanism results in the observed honeycomb microstructures.

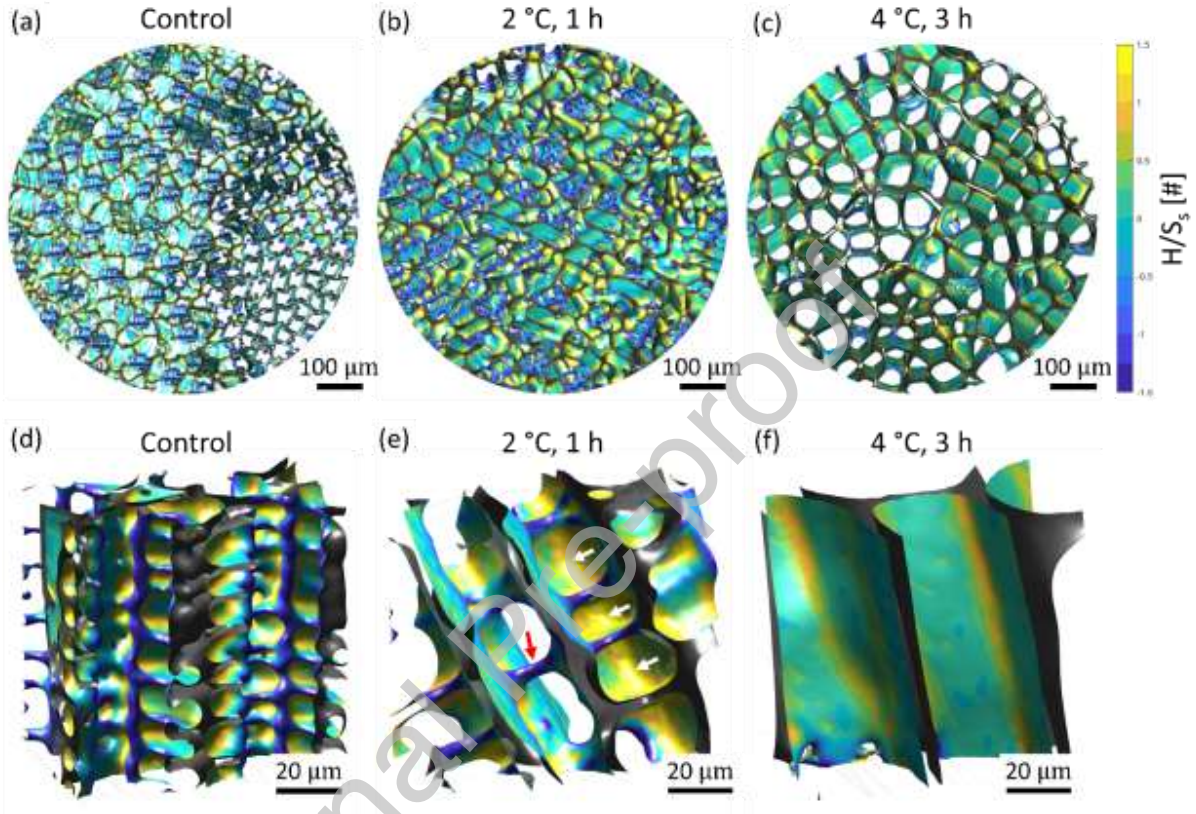

Fig. 5. 3D XCT reconstructions and subsections for the (a,d) control sample, (b,e) the sample coarsened at 2 °C for 1 h, and (c,f) sample coarsened at 4 °C for 3 h. The sides of the solid-pore interfaces that face the dendritic pores are colored according to the normalized mean curvature (H/S_s), as indicated by the colorbar in (c). White arrows in (e) show secondary pores with positive curvature caps, while the red arrow indicates a ligature with negative curvature.

3.4 Quantitative microstructure analysis

It is challenging to quantitatively compare highly complex microstructures using only 2D SEM images and visualizations of the 3D XCT reconstructions. A major advantage of the XCT technique is the ability to measure volumetric and interfacial properties. Metrics from the three XCT datasets are reported in Table 2. The pore volumes and volume fractions are similar between the three datasets. The porosity of all three samples was also measured using a modified Archimedes' method (ASTM C373). The two coarsened samples had nearly identical porosities using XCT and Archimedes' method. However, the 72% porosity of the control sample as measured by XCT, is believed to be slightly low due to expected difficulties in using X-rays to image finer-scale structures. The Archimedes-measured 76% porosity is more aligned with the other samples, and is thus reported in Table 2. The control sample contains ~17 times more interface area than the 2 °C coarsened sample, and ~25 times more interface area than the 4 °C coarsened sample. The inverse specific interface area (S_s^{-1}) is found to be equal to roughly half of the average secondary pore size. The control and 2 °C datasets have S_s^{-1} = 6.1 and 10.7 µm, and MIP-measured secondary pore size of 12.6 and 25.7 µm, respectively. The misalignment angles reported in Table 2 is a measurement of the angle between the average dendrite growth direction and the solidification direction (discussed in detail in section 3.5).

Table 2. Metrics from the three XCT datasets. S_s^{-1} is the inverse specific interface area, calculated as the total pore volume divided by the total solid-pore interface area. The misalignment angles correspond to the orientation domains observed in each sample.

Sample	Pore Volume [x10^7 µm^3]	Pore Volume Fraction [%]	Interface Area [x10^6 µm^2]	S_s^{-1} [µm]	Misalignment Angles [°]
Control	4.1	76*	67.0	6.1	~5, ~28
2 °C, 1 h	4.3	77	4.0	10.7	~35
4 °C, 3 h	4.2	75	2.7	15.6	~15, ~20, ~30

*Based upon Archemedes' measurements

Interface shape distributions (ISDs) are also used to quantitatively compare the complex microstructures. For example, ISDs have been used to compare anisotropic bone architectures with freeze-cast foams made for bone implants [54]. ISDs are contour maps that indicate the probability of finding an interfacial patch with a given pair of principal curvatures (κ_1/S_s and κ_2/S_s). Figs. 6a-c show the ISD generated from the XCT microstructures in Figs. 5a-c, respectively. A map of the possible shapes in ISDs is presented in Fig. 6d. ISDs are divided into four main regions, indicated by 1 to 4 in the Fig. 6d schematic. For dendritic porous materials:

- Region 1 contains patches with $\kappa_1 > 0$ and $\kappa_2 > \kappa_1$. These cap-like interfacial patches are concave toward the SiOC ceramic.
- Region 2 contains patches with $\kappa_1 < 0$ and $\kappa_2 > -\kappa_1$. These saddle-like patches are strongly curved toward the pores.
- Region 3 contains patches with $\kappa_1 < 0$ and $\kappa_2 < -\kappa_1$. These saddle-like patches are strongly curved toward the SiOC ceramic.

- Region 4 contains patches with $\kappa_1 < 0$ and $\kappa_2 > \kappa_1$. These cap-like interfacial patches are convex toward the SiOC ceramic.

Figs. 6e and 6f show the same section of the 2 °C coarsened dataset as in Fig. 5e, but the structures are colored according to interfacial shapes of interest. Patches with cylindrical shapes were isolated from the red-box region in the ISD in Fig. 6b and displayed on the microstructure in Fig. 6e. Most of these cylindrical features are primarily found along the walls of primary pores, but some patches are also present along the walls of secondary pores. The porous caps in the pink region of Fig. 6b are shown on the reconstruction in Fig. 6f. As expected, these high-curvatures features are mostly present at the tips of secondary pores.

A system is considered to be self-similar if the ISDs do not change during coarsening. The 2 °C and 4 °C ISDs are both different from the control ISD, thus coarsening is not taking place in a self-similar manner. This is somewhat surprising given that the previously mentioned $t^{1/3}$ power law holds. The major reason for lack of self-similarity is the disappearance of secondary arm tips and conversion to honeycomb structures. Compared to the control ISD (Fig. 6a), the 4 °C ISD (Fig. 6c) has a smaller probability in the top right section of Region 1 (pore caps) and a higher concentration of cylindrical patches (signal along $\kappa_1/S_s = 0$), consistent with the reconstructions shown in Fig. 5f.

The magnitude of the probability near the origin of the ISDs is indicative of the overall flatness of the microstructure. The control ISD has a yellow spot that extends to the saddle-like Regions 2 and 3. These interfaces are primarily found on the plate-like facets along the primary and secondary pores. The sample coarsened at 2 °C has a

peak shifted away from the origin. This is consistent with SEM images of decreased secondary pore length and ligature formation. The 4 °C ISD has the largest number of nearly flat interfaces, as expected from the honeycomb structures.

Since the dendrites in freeze casting undergo similar morphological evolution to cylinder-like shapes in alloy systems, the ISDs for the control sample and the sample coarsened at 4 °C for three hours are compared to the dendrite coarsening in Pb-Sn alloys reported by Cool and Voorhees [29,55,56]. The ISD of the control sample is similar to the ISD of the least-coarsened sample in the Cool and Voorhees study [55]. Both ISDs have peaks in the cylindrical and saddle regions as both structures contain significant amounts of interfacial patches from secondary arms or secondary pores. The freeze-cast and Pb-Sn ISDs are also similar when the structures are coarsened to cylindrical morphologies. Hence, the two systems exhibit similar general coarsening trends.

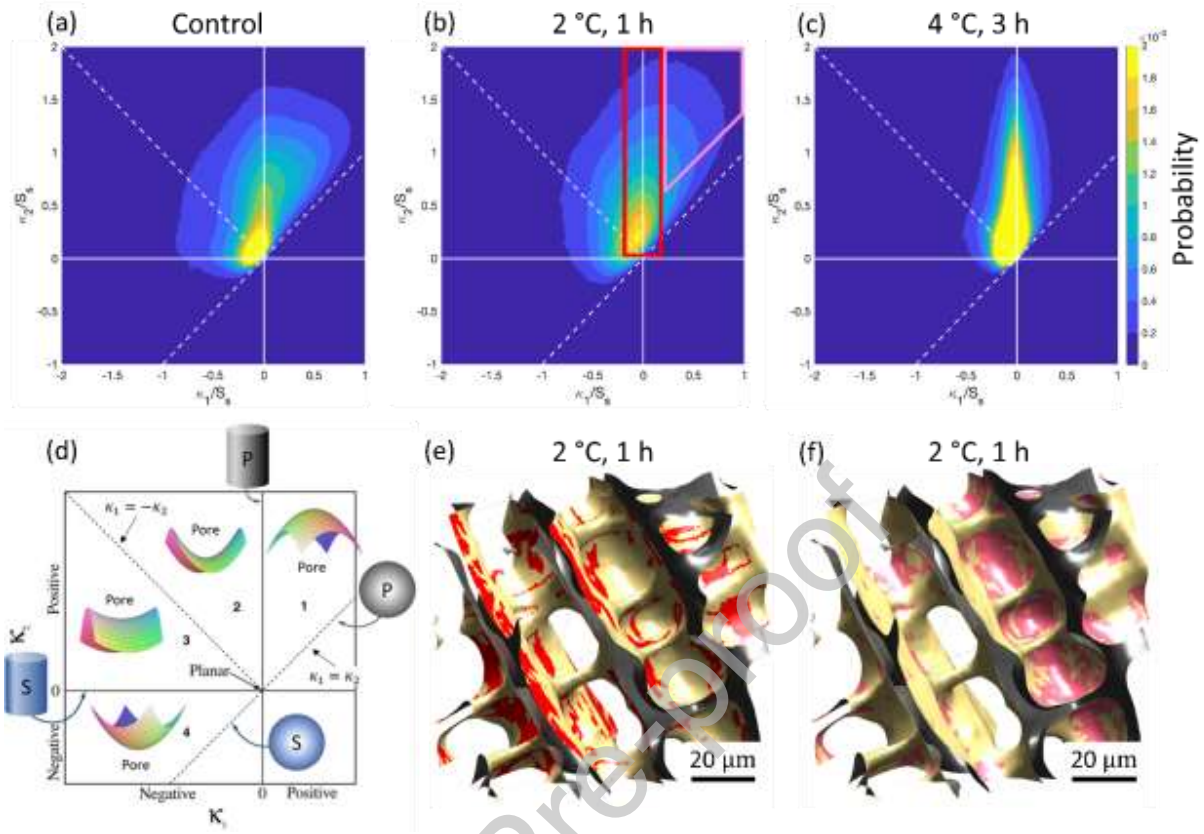

Fig. 6. Interface shape distributions (ISDs) for the (a) control sample, (b) sample coarsened at 2 °C for 1 h, and (c) sample coarsened at 4 °C for 3 h. (d) Map of the interface shapes possible in an ISD where P is pore and S is solid. This is a modified figure from ref. [57]. Sections of the 2 °C coarsened sample cylindrical patches colored in red (e) and porous caps colored in pink (f).

3.5 Directionality of dendritic pores

Directionality is of great interest because it influences transport [58] and mechanical properties [59] of freeze-cast solids. As clearly observed in the control XCT dataset (Fig. 5a) not all dendrites grow exactly perpendicular to the induced temperature gradient. Interface normal distributions (INDs) are used to quantitatively

measure the averaged dendritic growth directions [29,60–62]. For each of the three XCT datasets, normal vectors were calculated at each interfacial mesh face and their distributions were plotted on a hypersphere following the procedure outlined by Shahani [63]. The [001] stereographic projections are presented as INDs in Fig. 7 for the (a) control sample, (b) sample coarsened at 2 °C for one hour, and (c) sample coarsened at 4 °C for three hours. The IND center where the white lines intersect indicates the out of plane direction, parallel to the temperature gradient.

The IND for the control sample (Fig. 7a) is uniformly blue except for one spot (green arrow) at ~28° from the IND center. Some of the interfacial patches which contribute to this IND spot have been highlighted on the microstructure section in Fig. 7d. The green patches are primarily present on the relatively flat top faces of secondary pores. These interfaces have normal vectors that point in roughly the same direction, thus yielding a spot on the IND. Owing to the cubic symmetry of the system, the flat top faces are roughly perpendicular to the primary pore growth direction. Thus, the primary dendrites grew at ~28° from the temperature gradient direction. A rotation video of the entire control XCT dataset as viewed from the measured 28° tilt is available in the supplementary materials (Supplementary Video 7). At ~43 seconds into the video it is possible to view directly down many of the primary channels, confirming the angle measured in the IND.

The IND of the sample coarsened at 2 °C for 1 h (Fig. 7b) contains a spot (purple arrow) at ~35° from the center. This spot indicates the average misalignment of multiple domains within the sample. The microstructure section in Fig. 7e has purple patches corresponding to the spot in the IND. As in the control sample, these interfaces are

mostly present at secondary pores. The IND also has an arc-like band, marked by four red arrows and one blue arrow at the highest-intensity spot. Fig. 7f shows a section of the microstructure where patches that contribute to the IND spot (denoted by the blue arrow) are highlighted in blue. These areas are primarily found on the flatter regions of primary pores. The primary pores in the 2 °C coarsened sample have walls with normal vectors that point in many directions, all of them nearly perpendicular to the primary dendrite growth direction. This is manifested as an arc-band in the IND (red arrows in Fig. 7b). The band is tilted at ~55° away from the temperature gradient direction, and ~90° away from the secondary arm spot (purple arrow in Fig. 7b). Together, these observations indicate that the average dendrite growth misalignment for the 2 °C coarsened sample is ~35°. A video of the rotating XCT microstructure as viewed from the ~35° tilt is available in the supplementary materials (Supplementary Video 8). At ~19 seconds into the video it is indeed possible to see down many of the primary pores.

The IND of the sample coarsened at 4 °C for 3 h (Fig. 7c) contains many light-blue bands. The bands appear smeared largely because the honeycomb-like structure is composed of large channels, each with a slightly different orientation. Three main orientations are identified (red, yellow, and pink arrows), indicating misorientations of ~20°, ~15°, and ~30°, respectively (Table 2). A video of the rotating XCT microstructure as viewed from the ~20° tilt is available in the supplementary materials (Supplementary Video 9). At ~38 seconds, it is possible to view down many of the channels. The channel misalignments from the three XCT datasets are summarized in Table 2. The preferential directionality of coarsened dendrites was also characterized in alloy

systems [29]. In contrast, freeze-cast lamellar pores identified from INDs by Fife et al, show two peaks located 180° apart due to the plate-like pores [54].

The misalignment of dendritic pores is expected since dendrites were randomly oriented at nucleation. As the dendrites grow, misoriented dendrites tend to impinge on aligned dendrites and stop growing. However, some fraction of off-axis dendrites are retained. Although the misalignment of pores affects transport properties of freeze-cast solids, the overall directionality of dendrites could be controlled through careful selection and design of substrates. Nucleation control by a grain selector can be used in freeze casting to align dendritic pores and has been shown to improve the Darcian permeability constant more than 6-fold [58]. The wedge systems were also shown to be effective in aligning pores as demonstrated in other studies [64,65]. Another example was demonstrated by Munch et al., which freeze-cast with patterned substrate to control orientation of pores [66].

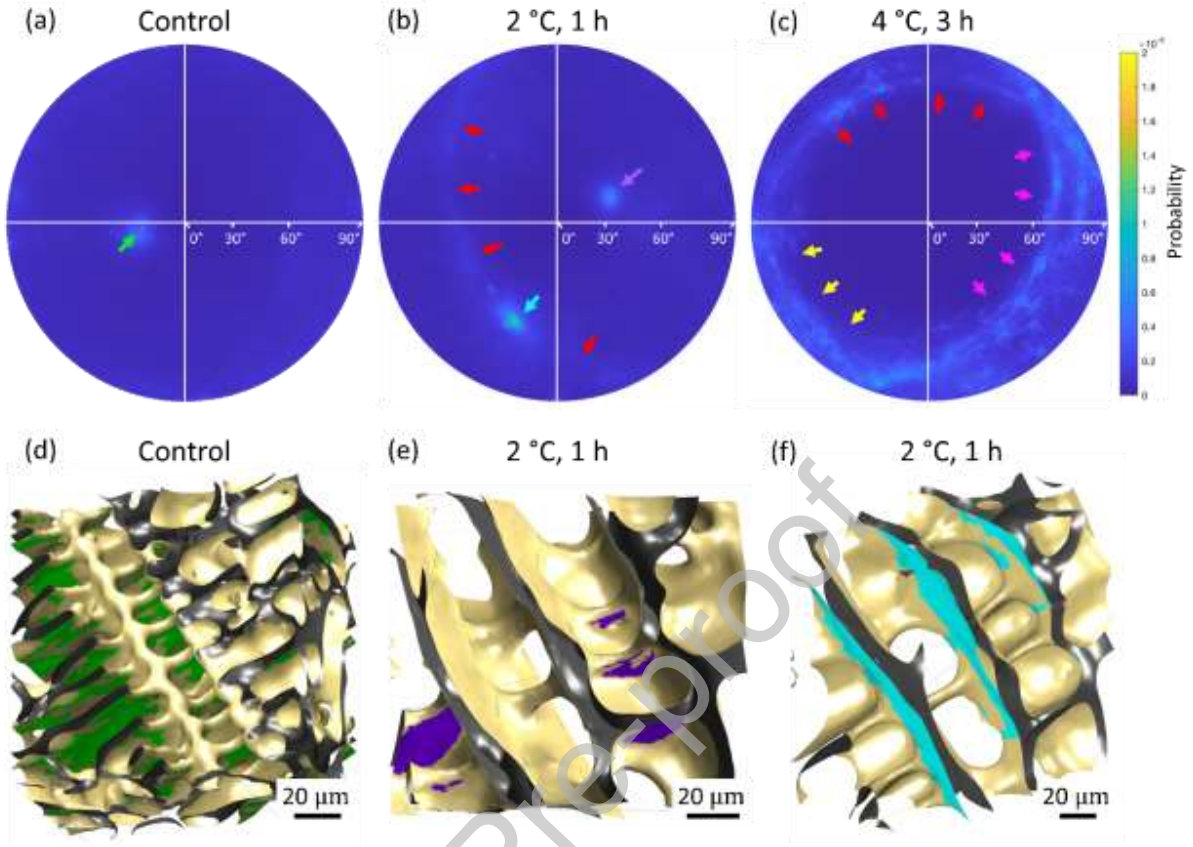

Fig. 7. Interface Normal Distributions (INDs) for the (a) control sample, (b) sample coarsened at 2 °C for 1 h, and (c) sample coarsened at 4 °C for 3 h. The green arrow in (a) corresponds to the green patches in (d). The purple arrow in (b) corresponds to purple patches in (e). The blue arrow in (b) corresponds to the blue patches in (f).

4. Discussion

4.1 Comparison with other alloy systems

The coarsening times in this study (up to five hours) are shorter than those in many alloy studies where dendrites were coarsened for several days (tens to thousands of hours) to observe the significant morphological change from dendrites to cylinders. Here, the freeze-cast system is compared with Pb-Sn alloys studied by Kammer and

Voorhees [29], where the dendrites evolve into cylinders after coarsening for ~48 hrs (nearly ten times longer than in the freeze-cast system). The model by Kirkwood for secondary arm coarsening [67] can be used to explain the faster morphological changes in freeze-cast systems:

$$\lambda = \left(-\frac{128D\sigma T_m}{LmC_L(1-k)}\right)^{1/3} t^{1/3} \qquad (5)$$

where λ is the secondary arm spacing, D is the diffusion coefficient of solute in the liquid, σ is the solid-liquid interface tension, T_m is the absolute melting temperature, L is the volumetric heat of fusion, m is the liquidus slope, C_L is the liquid composition, k is the partition coefficient, and t is the coarsening time. Although the values for some parameters such as D, σ, and C_L are not known for both the freeze-cast and alloy systems, a comparison of the known variables L and m provides insight into the differences in coarsening rates. L of eutectic Pb-Sn is ~300 J/cc, while that of pure cyclohexane is ~25 J/cc, which is an order of magnitude smaller. The absolute value of m for Sn-rich Pb-Sn alloys is ~1.4 °C/wt.%, while that of 0 wt.% to 40 wt.% preceramic polymer concentration ranges from 0.07 to 0.16 °C/wt.% [5], which is also an order of magnitude smaller. Both L and m are in the dominator of Eqn. 5, thus the smaller values for the freeze-cast system indicate a larger coarsening rate than in Pb-Sn alloys. Although further assessment of unknown variables is necessary to draw conclusions, the current analysis is consistent with the observed higher coarsening rate in the freeze-cast system based on the Kirkwood model.

4.2 Tailoring pore morphology using coarsening temperature

Coarsening time and coarsening temperature are two major parameters that can be used to tailor pore size and morphology. It was demonstrated that primary and secondary pore sizes linearly depend on the cube root of coarsening time ($t^{1/3}$). The higher coarsening temperature accelerated the morphological transition from dendrites to honeycomb-like structures and increased the average pore size. Changing the coarsening temperature may alter the diffusion coefficient. However, if the diffusion coefficient (D) follows an Arrhenius behavior [68], or a reptation model in the case of long-chained polymers, the temperature dependence of D is sufficiently small (less than 1 % increase) that it cannot account for the 70 % and 40 % increase in coarsening rate for primary and secondary pores, respectively, that occurs with coarsening at 4 °C compared to 2 °C. Instead, the enhanced coarsening rate with temperature is likely due to the increase in liquid volume fraction. When the coarsening temperature is increased, the liquid fraction increases, causing C_L to decrease. Furthermore, a decrease in C_L is expected to increase D [69]. Hence, the changes in C_L and D as a result of higher coarsening temperature accelerate the coarsening process.

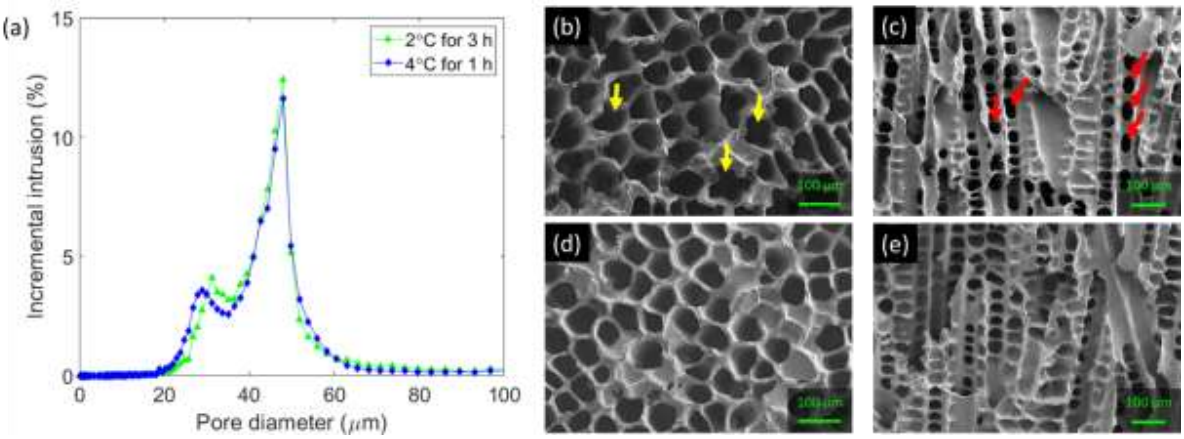

Fig. 8. (a) Pore size distribution from samples coarsened at 2 °C for 3 h and 4 °C for 1 h. Transverse and longitudinal SEM images of the samples coarsened at (b, c) 2 °C for 3 h, and (d, e) 4 °C for 1 h, respectively. Yellow arrows indicate primary pores with four-fold symmetry, and red arrows indicate thin tubes.

In addition to the aforementioned acceleration, the coarsening temperature could impact the freeze-cast morphology. This is highlighted in Fig. 8 where pore size distributions and SEM images are shown for samples coarsened at 2 °C for 3 h and 4°C for 1 h. As demonstrated using MIP, both samples have nearly identical pore size distributions, with marginally larger secondary pores present in the sample coarsened at 2 °C. The pore morphologies shown in SEM images, however, reveal distinct differences. In the transverse direction, some of the primary pores in the sample coarsened at 2 °C retain four-fold symmetry (yellow arrows in Fig. 8b), whereas the sample coarsened at 4 °C has a more honeycomb-like structure (Fig. 8d), changes which are likely to influence both tortuosity and permeability.

Additional differences are observed in the longitudinal direction. First, primary pores connect to neighboring primary pores by coalescence of secondary arms at 2 °C

(Fig. 8c). Second, some secondary pores are elliptical-shaped, as indicated by red arrows in Fig. 8c. Since the major axis of the ellipse is along the dendrite growth direction, it is likely that these large elliptical pores are result of coalescence of secondary arms that are nearly perpendicular to the dendrite growth direction. These large elliptical pores are likely what caused the slight shift of the secondary pore peak in the sample coarsened at 2 °C (Fig. 8a).

It is hypothesized that this morphological difference can be attributed to the difference in liquid fraction during coarsening. When samples were coarsened at 4 °C, close to the melting point of the solution, a sufficient fraction of the liquid phase was present to surround the dendrites, providing many pathways for mass diffusion. This allowed the structure to coarsen more uniformly, hence, both primary and secondary dendritic arms changed their morphologies which led to a larger secondary arm spacing. In contrast, at the lower 2 °C coarsening temperature, the lower volume fraction of liquid phase was more heterogeneously distributed throughout the microstructure. This led to preferential coalescence of some secondary arms, but an overall smaller secondary arm spacing. The discrepancy in coarsening mechanisms near individual dendrites results in a disparate coarsening behavior at different temperatures. These results further demonstrate that changing the coarsening temperature can be used to tailor the pore morphology and pore network.

5. Conclusion

This study demonstrates that coarsening can be applied to solution-based freeze casting to control the pore morphologies and sizes. The morphological evolution from

dendrites to cylindrical-like crystals was demonstrated in solution-based freeze casting, and ultimately resulted in honeycomb-like porous structures. We also show that both primary and secondary pore sizes scale with the cube root of coarsening time ($t^{1/3}$). Both findings are well-known in dendrite coarsening in metal alloy systems.

While many studies in freeze casting have focused on controlling crystal growth, to best of our knowledge, this is the first study to use X-ray tomography to quantitatively explore morphological evolution during coarsening of freeze-cast systems, specifically with interfacial shape distributions and interfacial normal distributions. ISDs were used quantitatively to determine that coarsened pore structures are not self-similar, similar to findings for coarsened dendrites in alloys [29,55]. INDs were used to quantitatively measure the preferential growth direction of pores, which is important for mechanical and transport properties of porous solids. Since the dendritic structures can be obtained by a variety of solvents, ISDs and INDs provide a useful platform to investigate morphological evolution of other dendritic structures. The current study validated that post-crystal growth processes, such as coarsening, offer an additional strategy to control and tailor the microstructures of freeze cast ceramics.

Acknowledgements

These studies were supported by the U.S. National Science Foundation under CBET-1911972 (NA, KTF), the U.S. Department of Commerce, National Institute of Standards and Technology as part of the Center for Hierarchical Materials Design (CHiMaD) under award number 70NANB19H005 (TS), the National Aeronautics and Space Administration under NNX16AR13G (PWV), and the U.S. Army Research Office Young

Investigator Program under W911NF-18-1-0162 (AJS). NSM and AJS acknowledge the University of Michigan College of Engineering for financial support and the Michigan Center for Materials Characterization for use of the instruments and staff assistance.

References

[1] E.C. Hammel, O.L.-R. Ighodaro, O.I. Okoli, Processing and properties of advanced porous ceramics: An application based review, Ceram. Int. 40 (2014) 15351–15370. https://doi.org/10.1016/j.ceramint.2014.06.095.

[2] A.R. Studart, U.T. Gonzenbach, E. Tervoort, L.J. Gauckler, Processing routes to macroporous ceramics: A review, in: J. Am. Ceram. Soc., Blackwell Publishing Inc, 2006: pp. 1771–1789. https://doi.org/10.1111/j.1551-2916.2006.01044.x.

[3] T. Ohji, M. Fukushima, Macro-porous ceramics: Processing and properties, Int. Mater. Rev. 57 (2012) 115–131. https://doi.org/10.1179/1743280411Y.0000000006.

[4] T. Waschkies, R. Oberacker, M.J. Hoffmann, Investigation of structure formation during freeze-casting from very slow to very fast solidification velocities, Acta Mater. 59 (2011) 5135–5145. https://doi.org/10.1016/j.actamat.2011.04.046.

[5] Maninpat Naviroj, Silicon-based Porous Ceramics via Freeze Casting of Preceramic Polymers (Ph.D. thesis), Northwestern University, 2017. https://search.proquest.com/openview/556ab0b3ba48bd5ad64aa2c67a18ff27/1?pq-origsite=gscholar&cbl=18750&diss=y (accessed May 23, 2018).

[6] S. Deville, Freezing Colloids: Observations, Principles, Control, and Use, Springer International Publishing, 2017. https://doi.org/10.1007/978-3-319-50515-2_1.

[7] S.H. Chen, B.H. Wu, J.C. Fu, G.J. Wang, L.S. Wan, Z.K. Xu, Vertically Oriented Microporous Membranes Prepared by Bidirectional Freezing, Chinese J. Polym. Sci. (English Ed. 36 (2018) 880–887. https://doi.org/10.1007/s10118-018-2113-z.

[8] M. Naviroj, P.W. Voorhees, K.T. Faber, Suspension- and solution-based freeze casting for porous ceramics, J. Mater. Res. 32 (2017) 3372–3382. https://doi.org/10.1557/jmr.2017.133.

[9] X. Zeng, N. Arai, K.T. Faber, Robust Cellular Shape-Memory Ceramics via Gradient-Controlled Freeze Casting, Adv. Eng. Mater. 21 (2019) 1900398. https://doi.org/10.1002/adem.201900398.

[10] M.M. Porter, R. Imperio, M. Wen, M.A. Meyers, J. McKittrick, Bioinspired scaffolds with varying pore architectures and mechanical properties, Adv. Funct. Mater. 24 (2014) 1978–1987. https://doi.org/10.1002/adfm.201302958.

[11] N. Arai, K.T. Faber, Hierarchical porous ceramics via two-stage freeze casting of preceramic polymers, Scr. Mater. 162 (2019) 72–76. https://doi.org/10.1016/j.scriptamat.2018.10.037.

[12] M.M. Porter, M. Yeh, J. Strawson, T. Goehring, S. Lujan, P. Siripasopsotorn, M.A. Meyers, J. Mckittrick, Magnetic freeze casting inspired by nature, Mater. Sci. Eng. A. 556 (2012) 741–750. https://doi.org/10.1016/j.msea.2012.07.058.

[13] S. Deville, E. Saiz, A.P. Tomsia, Freeze casting of hydroxyapatite scaffolds for

bone tissue engineering, Biomaterials. 27 (2006) 5480–5489. https://doi.org/10.1016/j.biomaterials.2006.06.028.
[14] Y. Tang, K. Zhao, L. Hu, Z. Wu, Two-step freeze casting fabrication of hydroxyapatite porous scaffolds with bionic bone graded structure, Ceram. Int. 39 (2013) 9703–9707. https://doi.org/10.1016/j.ceramint.2013.04.038.
[15] Y. Shao, M.F. El-Kady, C.W. Lin, G. Zhu, K.L. Marsh, J.Y. Hwang, Q. Zhang, Y. Li, H. Wang, R.B. Kaner, 3D Freeze-Casting of Cellular Graphene Films for Ultrahigh-Power-Density Supercapacitors, Adv. Mater. 28 (2016) 6719–6726. https://doi.org/10.1002/adma.201506157.
[16] Y. Liu, W. Zhu, K. Guan, C. Peng, J. Wu, Freeze-casting of alumina ultra-filtration membranes with good performance for anionic dye separation, Ceram. Int. 44 (2018) 11901–11904. https://doi.org/10.1016/j.ceramint.2018.03.160.
[17] H. Zhang, C.L. Fidelis, M. Wilhelm, Z. Xie, K. Rezwan, Macro/mesoporous SiOC ceramics of anisotropic structure for cryogenic engineering, Mater. Des. 134 (2017) 207–217. https://doi.org/10.1016/J.MATDES.2017.08.039.
[18] K.T. Faber, J.A. Kornfield, N.A. Arai, O. Bateman, R.F. Ismagilov, Freeze-cast ceramic membrane for size based filtration, International application number PCT/US2019/048005, 2019.
[19] S.M. Miller, X. Xiao, K.T. Faber, Freeze-cast alumina pore networks: Effects of freezing conditions and dispersion medium, J. Eur. Ceram. Soc. 35 (2015) 3595–3605. https://doi.org/10.1016/J.JEURCERAMSOC.2015.05.012.
[20] G. Oskam, Z. Hu, R.L. Penn, N. Pesika, P.C. Searson, Coarsening of metal oxide nanoparticles, Phys. Rev. E. 66 (114AD). https://doi.org/10.1103/PhysRevE.66.011403.
[21] S.C. Hardy, P.W. Voorhees, Ostwald ripening in a system with a high volume fraction of coarsening phase, Metall. Trans. A. 19 (1988) 2713–2721. https://doi.org/10.1007/BF02645806.
[22] J.L. Fife, P.W. Voorhees, The morphological evolution of equiaxed dendritic microstructures during coarsening, Acta Mater. 57 (2009) 2418–2428. https://doi.org/10.1016/j.actamat.2009.01.036.
[23] D. Kammer, R. Mendoza, P.W. Voorhees, Cylindrical domain formation in topologically complex structures, Scr. Mater. 55 (2006) 17–22. https://doi.org/10.1016/j.scriptamat.2006.02.027.
[24] P.W. Voorhees, The theory of Ostwald ripening, J. Stat. Phys. 38 (1985) 231–252. https://doi.org/10.1007/BF01017860.
[25] D. Fan, S.P. Chen, L.Q. Chen, P.W. Voorhees, Phase-field simulation of 2-D Ostwald ripening in the high volume fraction regime, Acta Mater. 50 (2002) 1895–1907. https://doi.org/10.1016/S1359-6454(01)00393-7.
[26] L.K. Aagesen, J.L. Fife, E.M. Lauridsen, P.W. Voorhees, The evolution of interfacial morphology during coarsening: A comparison between 4D experiments and phase-field simulations, Scr. Mater. 64 (2011) 394–397. https://doi.org/10.1016/j.scriptamat.2010.10.040.
[27] A.J. Shahani, X. Xiao, K. Skinner, M. Peters, P.W. Voorhees, Ostwald ripening of faceted Si particles in an Al-Si-Cu melt, Mater. Sci. Eng. A. 673 (2016) 307–320. https://doi.org/10.1016/j.msea.2016.06.077.
[28] E. Guo, A.B. Phillion, B. Cai, S. Shuai, D. Kazantsev, T. Jing, P.D. Lee, Dendritic

evolution during coarsening of Mg-Zn alloys via 4D synchrotron tomography, Acta Mater. 123 (2017) 373–382. https://doi.org/10.1016/j.actamat.2016.10.022.
[29] D. Kammer, P.W. Voorhees, The morphological evolution of dendritic microstructures during coarsening, Acta Mater. 54 (2006) 1549–1558. https://doi.org/10.1016/j.actamat.2005.11.031.
[30] E.B. Gulsoy, A.J. Shahani, J.W. Gibbs, J.L. Fife, P.W. Voorhees, Four-Dimensional Morphological Evolution of an Aluminum Silicon Alloy Using Propagation-Based Phase Contrast X-ray Tomographic Microscopy, Mater. Trans. 55 (2014) 161–164. https://doi.org/10.2320/matertrans.M2013225.
[31] O. Ludwig, M. Dimichiel, L. Salvo, M. Suéry, P. Falus, In-situ three-dimensional microstructural investigation of solidification of an Al-Cu alloy by ultrafast X-ray microtomography, Metall. Mater. Trans. A Phys. Metall. Mater. Sci. 36 (2005) 1515–1523. https://doi.org/10.1007/s11661-005-0243-8.
[32] N. Limodin, L. Salvo, E. Boller, M. Suéry, M. Felberbaum, S. Gailliègue, K. Madi, In situ and real-time 3-D microtomography investigation of dendritic solidification in an Al-10 wt.% Cu alloy, Acta Mater. 57 (2009) 2300–2310. https://doi.org/10.1016/j.actamat.2009.01.035.
[33] T.F. Bower, H.D. Brody, M.C. Flemings, Measurements of Solute Redistribution in Dendritic Solidification, Trans. Metall. Soc. AIME. 236 (1966) 624–633.
[34] S. Wu, L. Li, H. Xue, K. Liu, Q. Fan, G. Bai, J. Wang, Size Controllable, Transparent, and Flexible 2D Silver Meshes Using Recrystallized Ice Crystals as Templates, ACS Nano. 11 (2017) 9898–9905. https://doi.org/10.1021/acsnano.7b03821.
[35] X. Liu, M.N. Rahaman, Q. Fu, Oriented bioactive glass (13-93) scaffolds with controllable pore size by unidirectional freezing of camphene-based suspensions: Microstructure and mechanical response, Acta Biomater. 7 (2011) 406–416. https://doi.org/10.1016/j.actbio.2010.08.025.
[36] K.M. Pawelec, A. Husmann, S.M. Best, R.E. Cameron, Altering crystal growth and annealing in ice-templated scaffolds, J. Mater. Sci. 50 (2015) 7537–7543. https://doi.org/10.1007/s10853-015-9343-z.
[37] A.J. Shahani, X. Xiao, E.M. Lauridsen, P.W. Voorhees, Characterization of metals in four dimensions, Mater. Res. Lett. 8 (2020) 462–476. https://doi.org/10.1080/21663831.2020.1809544.
[38] D. Paganin, S.C. Mayo, T.E. Gureyev, P.R. Miller, S.W. Wilkins, Simultaneous phase and amplitude extraction from a single defocused image of a homogeneous object, J. Microsc. 206 (2002) 33–40. https://doi.org/10.1046/j.1365-2818.2002.01010.x.
[39] N. Otsu, THRESHOLD SELECTION METHOD FROM GRAY-LEVEL HISTOGRAMS., IEEE Trans Syst Man Cybern. SMC-9 (1979) 62–66. https://doi.org/10.1109/TSMC.1979.4310076.
[40] T. Stan, Z.T. Thompson, P.W. Voorhees, Optimizing convolutional neural networks to perform semantic segmentation on large materials imaging datasets: X-ray tomography and serial sectioning, Mater. Charact. 160 (2020) 110119. https://doi.org/10.1016/j.matchar.2020.110119.
[41] T. Stan, Z. Thompson, P. Voorhees, Building towards a universal neural network to segment large materials science imaging datasets, in: B. Müller, G. Wang

(Eds.), Dev. X-Ray Tomogr. XII, SPIE-Intl Soc Optical Eng, 2019: p. 49. https://doi.org/10.1117/12.2525290.
[42] D.-J. Kroon, Smooth Triangulated Mesh - File Exchange - MATLAB Central, (2010). https://www.mathworks.com/matlabcentral/fileexchange/26710-smooth-triangulated-mesh (accessed February 15, 2021).
[43] M. Naviroj, S.M. Miller, P. Colombo, K.T. Faber, Directionally aligned macroporous SiOC via freeze casting of preceramic polymers, J. Eur. Ceram. Soc. 35 (2015) 2225–2232. https://doi.org/10.1016/j.jeurceramsoc.2015.02.013.
[44] V. Naglieri, P. Colombo, Ceramic microspheres with controlled porosity by emulsion-ice templating, J. Eur. Ceram. Soc. (2017). https://doi.org/10.1016/j.jeurceramsoc.2017.02.033.
[45] Y. Shao, G. Hoang, T.W. Zerda, Solid-solid phase transitions of cyclohexane in porous sol-gel glass, J. Non. Cryst. Solids. 182 (1995) 309–314. https://doi.org/10.1016/0022-3093(94)00527-3.
[46] M. Wojdyr, Fityk: A general-purpose peak fitting program, J. Appl. Crystallogr. 43 (2010) 1126–1128. https://doi.org/10.1107/S0021889810030499.
[47] M. Chen, T.Z. Kattamis, Dendrite coarsening during directional solidification of Al-Cu-Mn alloys, Mater. Sci. Eng. A. 247 (1998) 239–247. https://doi.org/10.1016/s0921-5093(97)00720-x.
[48] S.C. Huang, M.E. Glicksman, Overview 12: Fundamentals of dendritic solidification-II development of sidebranch structure, Acta Metall. 29 (1981) 717–734. https://doi.org/10.1016/0001-6160(81)90116-4.
[49] T. Cool, P.W. Voorhees, Dendrite fragmentation: an experiment-driven simulation, Philos. Trans. R. Soc. A Math. Phys. Eng. Sci. 376 (2018) 20170213. https://doi.org/10.1098/rsta.2017.0213.
[50] H. Neumann-Heyme, K. Eckert, C. Beckermann, General evolution equation for the specific interface area of dendrites during alloy solidification, Acta Mater. 140 (2017) 87–96. https://doi.org/10.1016/j.actamat.2017.08.021.
[51] C. Yang, L. Liu, X. Zhao, Y. Li, J. Zhang, H. Fu, Dendrite morphology and evolution mechanism of nickel-based single crystal superalloys grown along the <001> and <011> orientations, Prog. Nat. Sci. Mater. Int. 22 (2012) 407–413. https://doi.org/10.1016/j.pnsc.2012.10.001.
[52] C.A. Gandin, M. Eshelman, R. Trivedi, Orientation dependence of primary dendrite spacing, Metall. Mater. Trans. A Phys. Metall. Mater. Sci. 27 (1996) 2727–2739. https://doi.org/10.1007/BF02652367.
[53] R.N. Grugel, Y. Zhou, Primary dendrite spacing and the effect of off-axis heat flow, Metall. Trans. A. 20 (1989) 969–973. https://doi.org/10.1007/BF02651662.
[54] J.L. Fife, J.C. Li, D.C. Dunand, P.W. Voorhees, Morphological analysis of pores in directionally freeze-cast titanium foams, J. Mater. Res. 24 (2009) 117–124. https://doi.org/10.1557/jmr.2009.0023.
[55] T. Cool, P.W. Voorhees, The evolution of dendrites during coarsening: Fragmentation and morphology, Acta Mater. 127 (2017) 359–367. https://doi.org/10.1016/j.actamat.2017.01.029.
[56] D. Kammer, R. Mendoza, P.W. Voorhees, Cylindrical domain formation in topologically complex structures, Scr. Mater. 55 (2006) 17–22. https://doi.org/10.1016/j.scriptamat.2006.02.027.

[57] J.L. Fife, J.W. Gibbs, E.B. Gulsoy, C.L. Park, K. Thornton, P.W. Voorhees, The dynamics of interfaces during coarsening in solid-liquid systems, Acta Mater. 70 (2014) 66–78. https://doi.org/10.1016/j.actamat.2014.01.024.
[58] M. Naviroj, M.M. Wang, M.T. Johnson, K.T. Faber, Nucleation-controlled freeze casting of preceramic polymers for uniaxial pores in Si-based ceramics, Scr. Mater. 130 (2017) 32–36. https://doi.org/10.1016/j.scriptamat.2016.10.038.
[59] A. Lichtner, D. Roussel, D. Jauffrès, C.L. Martin, R.K. Bordia, Effect of Macropore Anisotropy on the Mechanical Response of Hierarchically Porous Ceramics, J. Am. Ceram. Soc. 99 (2016) 979–987. https://doi.org/10.1111/jace.14004.
[60] R. Mendoza, J. Alkemper, P.W. Voorhees, The morphological evolution of dendritic microstructures during coarsening, Metall. Mater. Trans. A Phys. Metall. Mater. Sci. 34 A (2003) 481–489. https://doi.org/10.1007/s11661-003-0084-2.
[61] D.J. Rowenhorst, A. Gupta, C.R. Feng, G. Spanos, 3D Crystallographic and morphological analysis of coarse martensite: Combining EBSD and serial sectioning, Scr. Mater. 55 (2006) 11–16. https://doi.org/10.1016/j.scriptamat.2005.12.061.
[62] G.S. Rohrer, D.M. Saylor, B. El Dasher, B.L. Adams, A.D. Rollett, P. Wynblatt, The distribution of internal interfaces in polycrystals, Zeitschrift Für Met. 95 (2004) 197–214. https://doi.org/10.3139/146.017934.
[63] A.J. Shahani, Interfacial Evolution in Four Dimensions: Growth and Coarsening in Highly Anisotropic Systems (Ph.D. thesis), Northwestern University, 2016.
[64] H. Bai, Y. Chen, B. Delattre, A.P. Tomsia, R.O. Ritchie, Bioinspired large-scale aligned porous materials assembled with dual temperature gradients, Sci. Adv. 1 (2015). https://doi.org/10.1126/sciadv.1500849.
[65] M.W. Pot, K.A. Faraj, A. Adawy, W.J.P. Van Enckevort, H.T.B. Van Moerkerk, E. Vlieg, W.F. Daamen, T.H. Van Kuppevelt, Versatile wedge-based system for the construction of unidirectional collagen scaffolds by directional freezing: Practical and theoretical considerations, ACS Appl. Mater. Interfaces. 7 (2015) 8495–8505. https://doi.org/10.1021/acsami.5b00169.
[66] E. Munch, E. Saiz, A.P. Tomsia, S. Deville, Architectural Control of Freeze-Cast Ceramics Through Additives and Templating, J. Am. Ceram. Soc. 92 (2009) 1534–1539. https://doi.org/10.1111/j.1551-2916.2009.03087.x.
[67] D.H. Kirkwood, A simple model for dendrite arm coarsening during solidification, Mater. Sci. Eng. 73 (1985) L1. https://doi.org/10.1016/0025-5416(85)90319-2.
[68] L. Cai, J. Lu, Z. Gao, Z. Cai, Dynamic Analysis Model for the Diffusion Coefficient in High-Viscosity Polymer Solution, Ind. Eng. Chem. Res. 57 (2018) 15924–15934. https://doi.org/10.1021/acs.iecr.8b03966.
[69] J.S. Vrentas, J.L. Duda, Diffusion in polymer–solvent systems. II. A predictive theory for the dependence of diffusion coefficients on temperature, concentration, and molecular weight, J. Polym. Sci. Polym. Phys. Ed. 15 (1977) 417–439. https://doi.org/10.1002/pol.1977.180150303.